*Advanced Functional Materials*

ADVANCED FUNCTIONAL MATERIALS
www.afm-journal.de

RESEARCH ARTICLE

# Giant Negative Photoconductivity in a Van Der Waals Heterojunction-Based FET with Bidirectional Photoresponse

Hongzhi Guo[1] | Zhaotan Gao[1] | Zhili Cheng[1] | Ruiqi Jiang[1] | Zhuojing Du[1] | Dan Mou[1] | Yawei Li[1] | Liyan Shang[1] | Liangqing Zhu[1] | Shuiyuan Wang[2,3] | Jinzhong Zhang[1] | Zhigao Hu[1,4] | Junhao Chu[1,2]

[1]Technical Center for Multifunctional Magneto-Optical Spectroscopy (Shanghai), Engineering Research Center of Nanophotonics & Advanced Instrument (Ministry of Education), Department of Physics, East China Normal University, Shanghai, China | [2]State Key Laboratory of Integrated Chips and Systems (SKLICS), College of Integrated Circuits and Micro-Nano Electronics, Fudan University, Shanghai, China | [3]Shaoxin Laboratory, Shaoxing, Zhejiang, China | [4]Collaborative Innovation Center of Extreme Optics, Shanxi University, Taiyuan, Shanxi, China

**Correspondence:** Liyan Shang (lyshang@ee.ecnu.edu.cn) | Jinzhong Zhang (jzzhang@ee.ecnu.edu.cn)

**Received:** 29 October 2025 | **Revised:** 30 December 2025 | **Accepted:** 10 April 2026

**Keywords:** artificial synapses | bidirectional photoresponse | giant negative photoconductivity | information protection | $WSe_2$/UVO-InSe heterojunction

## ABSTRACT

Phototransistors with the bidirectional photoresponse (positive and negative photoconductivity, PPC and NPC) have broad prospects for novel and multifunctional applications. Herein, a novel strategy is proposed to achieve bidirectional photoresponse in a vertical $WSe_2$/UVO-InSe field-effect transistor (FET) with ultraviolet-ozone (UVO) oxidized InSe nanosheets. It exhibits a giant NPC performance with a high $I_{OFF}/I_{ON}$ ratio ($6.32 \times 10^5$), responsivity ($R_{NPC} = -1.56 \times 10^5$ A W$^{-1}$) and remarkable operational stability. In a further step, the separation-transport-recombination process of photogenerated carriers has been investigated under various gate voltages for the physical mechanism of bidirectional photoconductivity. Particularly, the accumulation and recombination of electrons and holes at the $WSe_2$/UVO-InSe interface could induce the giant NPC effect. Moreover, information protection and pattern recognition systems are realized based on the PPC and NPC effects. This study highlights the promising potential of the van der Waals heterojunction-based FETs with bidirectional photoresponse for multifunctional optoelectronic devices.

## 1 | Introduction

Phototransistors, as critical components of optoelectronic devices, play an important role in the fields of image sensing, optical communications, and photodetection [1–4]. Their photoelectric performance directly influences the overall functionality and efficiency of related equipment [5, 6]. Phototransistors with bidirectional photoresponse (i.e., positive and negative photoconductivity, PPC, and NPC) demonstrate significant application potential in artificial synapse, information encryption, secure data transmission, signal processing in complex optical environment and multifunctional optoelectronic integrated systems [7–13]. In particular, the intrinsic switch between PPC and NPC provides a natural foundation for implementing optical information protection, which is highly desirable for next-generation information security applications [14, 15]. The advancement offers possibilities for the diversified development of photoelectronic technology.

Recently, the NPC effect has been demonstrated in some material systems such as 2D layered materials, halide perovskites, low-dimensional nanomaterials, and organic semiconductors [16–19].

Hongzhi Guo and Zhaotan Gao have contributed equally to this work.

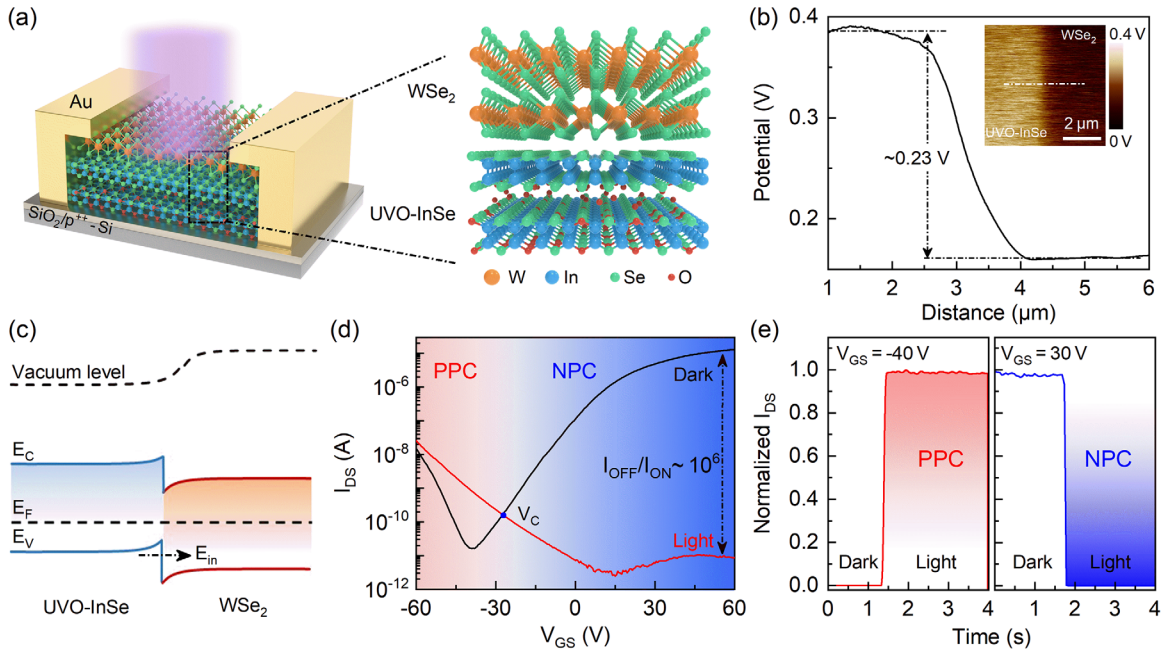


**FIGURE 1** | Structure and bidirectional photoresponse of the $WSe_2$/UVO-InSe heterojunction-based FET. (a) Schematic diagram of the FET based on the vertical $WSe_2$/UVO-InSe heterojunction. (b) Surface potential difference of the $WSe_2$/UVO-InSe heterojunction. (c) Schematic band structure of the $WSe_2$/UVO-InSe heterojunction at $V_{GS} = 0$ V. (d) Transfer characteristic curves under dark and 405 nm-laser illumination at $V_{DS} = 1$ V. (e) Photocurrent responses by applying different gate voltages ($V_{GS} = -40$ V $< V_C$ and 30 V $> V_C$).

For example, Grillo et al. realized PPC and NPC in a $PtSe_2$-based transistor due to the light-induced oxygen desorption [17]. Cai et al. presented an all-optically controlled retinomorphic memristor based on the halide perovskite ($Cs_xFA_yMA_{1-x-y}Pb(I_zBr_{1-z})_3$), where the bidirectional photoresponse is tuned by laser power density [20]. Qin et al. reported the first observation of the NPC effect in carbon dots [21]. Moreover, a simple fully light-modulated artificial synaptic device based on SnSe films is constructed to operate various synaptic plasticity and reversible modulation of conductance under 430 and 255 nm illuminations [16]. However, achieving bidirectional photoresponse with high responsivity and photosensitivity presents significant challenges. Compared with the PPC effect, achieving pronounced NPC is difficult by tuning carrier transport in semiconductors [22]. Moreover, there exists a fundamental physical mechanism contradiction in simultaneously enhancing NPC and a high detection sensitivity. These limitations restrict the applications of photodetection, secure information processing, neuromorphic computing, etc.

2D-layered materials have promising potential for optoelectronic devices due to the tunable bandgap, high carrier mobility, stability, excellent mechanical flexibility, etc [23–26]. Moreover, atomic-level interface regulation and adjustable band structures provide the prerequisite of bidirectional photoresponse [27, 28]. Compared with other 2D-layered semiconductors, ambipolar-$WSe_2$, n-type InSe, and p-type ultraviolet-ozone InSe (UVO-InSe) have an excellent photoelectric stability and unique bandgap alignment for high-performance optoelectronic devices for bidirectional photoresponse-enabled information protection [29–31]. High-efficiency photoelectric sensor arrays based on the 2D $MoS_2$ and $WSe_2$ have been developed for artificial vision systems [32]. Furthermore, vertical heterojunctions have a more efficient carrier regulation ability due to the formation of built-in electric field at the interface, which could induce a giant NPC [33, 34]. The heterojunction interface states can be regulated by van der Waals stacking, molecular beam epitaxy (MBE), and UVO treatment [35–37]. Note that the UVO technique is a simple and effective surface modification method to introduce electron states above the valence bands [37, 38].

In this work, a vertical van der Waals heterojunction-based FET was fabricated by stacking $WSe_2$ and UVO-treated InSe nanosheets, which exhibits both PPC and NPC effects by applying different gate voltages. Particularly, it exhibits a giant negative photoconductivity ($I_{OFF}/I_{ON} = 6.32 \times 10^5$) and high responsivity ($R_{NPC} = -1.56 \times 10^5$ A W$^{-1}$) at $V_{GS} = 30$ V. Furthermore, the separation/recombination and transport processes of photogenerated carriers have been investigated under various gate voltages for the physical mechanism of bidirectional photoresponse. The transport and recombination of electrons and holes at the $WSe_2$/UVO-InSe interface could induce the giant NPC performance. Finally, the gate-tunable bidirectional photoresponse is exploited for information protection and pattern recognition.

## 2 | Results and Discussion

### 2.1 | Structure and Bidirectional Photoresponse of $WSe_2$/UVO-InSe FETs

Figure 1a and Figure S1a show that $WSe_2$ and UVO-InSe nanosheets are vertically stacked to form a heterojunction. The thicknesses of $WSe_2$ and UVO-InSe nanosheets are about 16 nm and 7.5 nm, respectively (cf. Figure S1b). Note that UVO treatment

induces the oxygen atoms into the InSe interlayer at the bottom surface nearby $SiO_2$. The UVO-InSe has a p-type conductivity based on the transfer characteristic curves and surface potential differences (cf. Figures S2 and S3). In Figure 1b, there exists a potential difference of about 0.23 V between UVO-InSe and $WSe_2$ nanosheets, which indicates that a built-in electric field ($E_{in}$) is formed at the $WSe_2$/UVO-InSe interface. Figure 1c illustrates the band alignment of $WSe_2$ and UVO-InSe according to their work functions and bandgaps, which belongs to the type-II heterojunction [39–41]. The interface carrier recombination strongly predicts a possibility of electrical modulation for the PPC and NPC in the type-II $WSe_2$/UVO-InSe heterojunction. The carrier recombination at the heterojunction interface is dominated, which is confirmed by the time-resolved photoluminescence (cf. Figure S1d). In Figure 1d, the transfer characteristic curves of $WSe_2$/UVO-InSe heterojunction-based FETs reveal an ambipolar characteristic under dark and illumination. It should be emphasized that the photocurrent is lower than dark current at $V_{GS} > V_C$. Here, $V_C$ is the critical gate voltage of the transition between PPC and NPC. The X-ray photoelectron spectroscopy spectra (XPS) of UVO-InSe nanosheets show that the oxide species increase progressively with increasing the UVO-exposure time, and the NPC performance of $WSe_2$/UVO-InSe FETs appears (cf. Figure S4). On the contrary, the photocurrent is higher than dark current at $V_{GS} < V_C$. It means that the $WSe_2$/UVO-InSe heterojunction-based FETs could exhibit PPC or NPC performance by applying a certain gate voltage. Furthermore, Figure 1e depicts the time-dependent channel current before and during illumination at the gate voltages of -40 and 30 V. It indicates a gate-tunable bidirectional photoresponse in the vertical $WSe_2$/UVO-InSe heterojunction-based FETs. Note that the large gate voltage will not induce a high power consumption due to the low leakage current ($I_{GS} \sim 10^{-14}$ A). Moreover, the gate voltage will decrease dramatically for the case of a thin high-k dielectric layer in the transistors. The FETs based on the $WSe_2$/InSe without UVO exposure fail to exhibit gate-tunable bidirectional photoresponse, indicating that the UVO treatment results in the NPC effect (cf. Figure S5).

## 2.2 | Gate-Tunable PPC and NPC of $WSe_2$/UVO-InSe FETs

Figure 2a shows the transfer characteristic curves of a $WSe_2$/UVO-InSe heterojunction-based FET under various 405 nm-laser power densities from 0 to 15.2 mW $cm^{-2}$ and it displays an ambipolar behavior under dark. The device has a giant NPC effect at weak laser power density by applying a large positive gate voltage. And it has a high PPC at the high laser power density by applying a certain negative gate voltage (cf. Figure 2b). As the gate voltage increases from −60 to +60 V, the PPC effect is observed, then the NPC effect is enhanced and tends to saturate. Therefore, the PPC and NPC effects could be modulated by gate voltages under illumination. In addition, the FET exhibits gate-tunable bidirectional photoresponse by applying different laser wavelengths (520 and 638 nm), as shown in Figure S6. The positive and negative photosensitivities at different laser power densities show a similar feature. The $I_{Light}/I_{Dark}$ increases as the laser power density increases by applying a negative gate voltage. In addition, the critical gate-voltage ($V_C$) at various laser power densities has a shift toward positive gate voltage, which means $V_C$ could be effectively tuned by the laser power intensity (Figure S7). In Figure 2c, the photocurrent increases as the laser power density increases at $V_{GS} = -40$ V due to the well-known photoelectric effect, which shows a good Ohmic contact formed between the channel and electrodes. For the case of $V_{GS} = 30$ V, the photocurrent is smaller than the dark current even though it increases with the laser power density (cf. Figure 2d). The nonlinear $I_{DS}$–$V_{DS}$ curves reveal a Schottky contact between the channel and electrodes by applying the positive gate voltage. In a further step, the fundamental charge transports at $V_{GS} = -40$ V (PPC) and 30 V (NPC) are confirmed by the temperature-dependent $I_{DS}$–$V_{DS}$ measurements (cf. Figure S8). Moreover, the time-dependence of channel current in Figure 2e,f shows that the FET has stable PPC and NPC behaviors at certain gate voltages, respectively. The PPC increases with the laser power density at a negative gate voltage ($V_{GS} = -40$ V), while NPC decreases with the laser power density at a positive gate voltage ($V_{GS} = 30$ V). Furthermore, the rise time ($\tau_r$), fall time ($\tau_d$), and switching speed ($\tau < 51.1$ ms) of the PPC ($\tau_r = 12.1$ ms and $\tau_d = 26.8$ ms) and NPC ($\tau_r < 82.7$ ms and $\tau_d = 130.3$ ms) states were obtained (cf. Figure S9). A reversible cycle of PPC and NPC effects could be realized by applying a certain gate voltage (cf. Figure S10). Note that the photocurrent cannot return to the initial state (dark current) after illumination and it can be reset by a negative gate voltage (cf. Figure S11).

## 2.3 | Stability of Giant NPC in $WSe_2$/UVO-InSe FETs

In Figure 3a, the NPC of a $WSe_2$/UVO-InSe heterojunction-based FET has been repeatedly measured for more than two months. It suggests that the NPC performance does not decay obviously, which is confirmed by the corresponding $I_{OFF}/I_{ON}$ (cf. Figure S12a). The as-fabricated phototransistor has a stable NPC performance according to the photoresponse of different devices and different cycles data, as well as retention curves (cf. Figure S12c–e). Figure 3b shows that the off-state current ($I_{OFF}$) is around $2 \times 10^{-6}$ A and the on-state current ($I_{ON}$) remains stable nearby $3 \times 10^{-12}$ A. Therefore, the value of $I_{OFF}/I_{ON}$ is located in the range of $5 \times 10^5 \sim 8 \times 10^5$ in the cycle-to-cycle test (cf. Figure 3c). The phototransistor exhibits an excellent reliability, maintaining a stable performance without noticeable degradation after 1000 continuous off/on cycles. The statistical distribution of device-to-device test indicates that more than 90% devices have a giant NPC ($I_{OFF}/I_{ON} > 10^5$), as shown in Figure 3d. The statistical distribution of $I_{OFF}/I_{ON}$ reveals that the $WSe_2$/UVO-InSe heterojunction-based FETs have excellent NPC repeatability. In addition, the device also has a stable PPC performance (cf. Figure S13).

In Figure 3e, a giant NPC ($IOFF/I_{ON} > 10^5$) could be obtained by applying a weak laser power density and a gate voltage ($V_{GS} = 30$ V). The corresponding power consumption is around 54 pJ per laser pulse based on the following equations: $E = P_{in} \times A_{device} \times T_{duration}$. Here, $P_{in}$, $A_{device}$ and $T_{duration}$ are the laser power density ($P_{in} = 0.03$ mW $cm^{-2}$), effective channel area (36 $\mu m^2$) and pulse duration (5 s), respectively [48]. In a further step, the NPC performance at various laser power densities is characterized by responsivity, which is derived from the following formula [19, 22]: $R = I_{ph}/(P_{in} \cdot A_{device})$. Here, $I_{ph} = I_{Light}$-$I_{Dark}$, $P_{in}$ is the laser

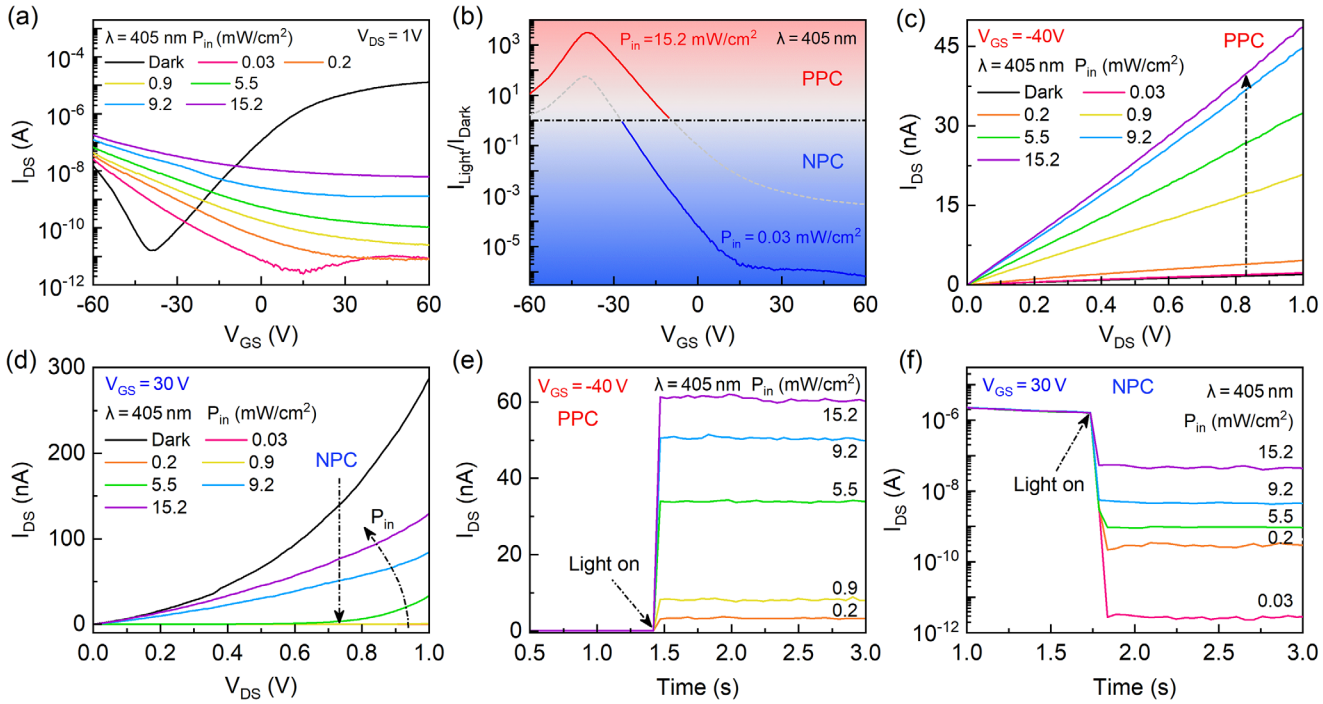


**FIGURE 2** | Photoelectric performance of a $WSe_2$/UVO-InSe heterojunction-based FET illuminated by the 405 nm-laser. (a) Transfer characteristic curves at the various 405 nm-laser power densities from 0.03 to 15.2 mW $cm^{-2}$ at $V_{DS} = 1$ V. (b) $I_{Light}/I_{Dark}$ as a function of gate voltage ($P_{in} = 0.03$ and 15.2 mW $cm^{-2}$). Output characteristic curves at various laser power densities by applying (c) $V_{GS}$ = -40 V and (d) $V_{GS} = 30$ V. The corresponding laser power density dependence of current ($V_{DS} = 1$ V) at (e) $V_{GS} = -40$ V and (f) $V_{GS} = 30$ V.

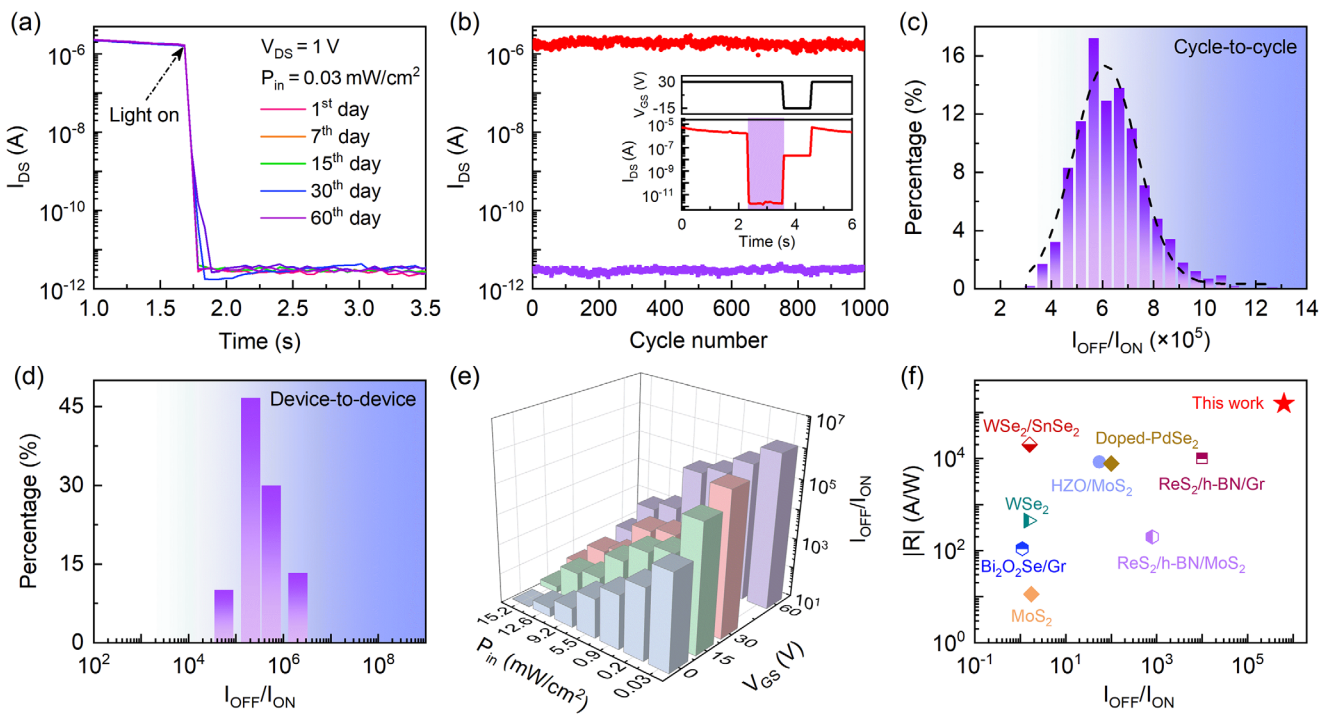


**FIGURE 3** | NPC performance stability of $WSe_2$/UVO-InSe heterojunction-based FETs. (a) The FET NPC stability for a period of time. (b) Time-dependent photoresponse of the FET in 1000 off/on cycles and (c) the corresponding statistical distribution of $I_{OFF}/I_{ON}$. Inset: the reset operation. (d) Statistical distribution of $I_{OFF}/I_{ON}$ for 30 FETs. (e) $I_{OFF}/I_{ON}$ as functions of laser power density ($P_{in}$) and gate voltage ($V_{GS}$). (f) Comparison of $|R_{NPC}|$ and $I_{OFF}/I_{ON}$ reported in literature [18, 27, 42–47].

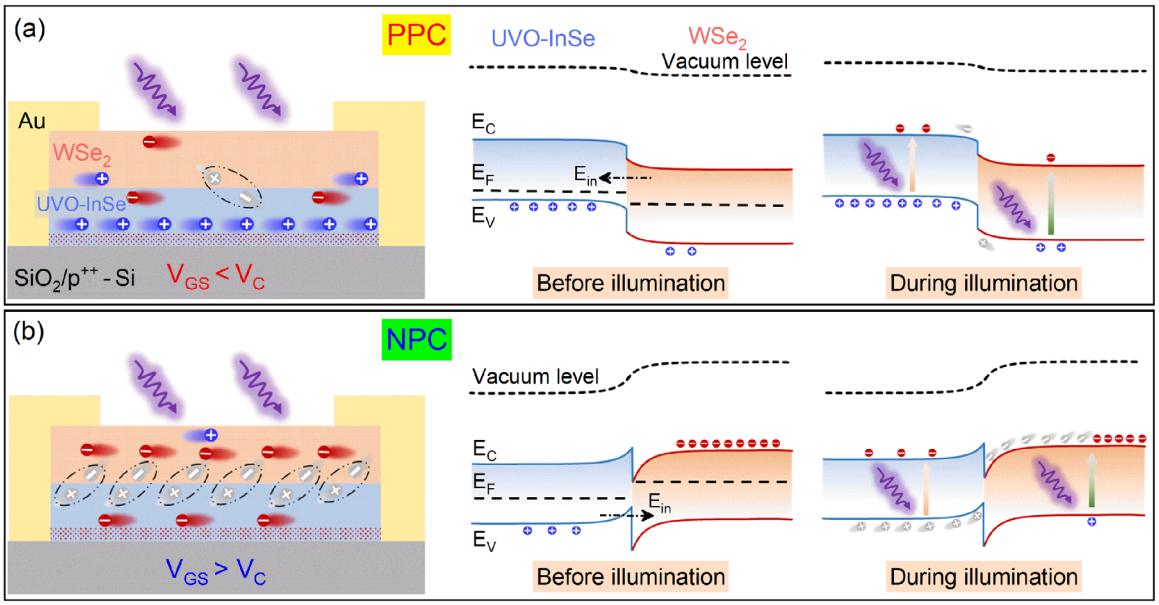


**FIGURE 4** | Mechanism diagram of the FET based on the vertical $WSe_2$/UVO-InSe heterojunction. Schematic illustration of carrier transports and the corresponding band alignments in the $WSe_2$/UVO-InSe heterojunction-based FET at (a) $V_{GS} < V_C$ and (b) $V_{GS} > V_C$.

power density (0.03 mW cm$^{-2}$), and $A_{device}$ represents the effective channel area (36 μm$^2$) of the FET (cf. Figure S14). In Figure 3f and Figure S15, the values of negative responsivity ($-1.56 \times 10^5$ A W$^{-1}$) and $I_{OFF}/I_{ON}$ ($6.32 \times 10^5$) for the $WSe_2$/UVO-InSe heterojunction-based FETs suggest an excellent NPC performance compared with those of other devices reported in the literature [18, 27, 42–47]. The values of specific detectivity (D*) and external quantum efficiency (EQE) of NPC are about $5.4 \times 10^{13}$ Jones and $4.7 \times 10^7$%, respectively (Figure S16). For the case of PPC performance, the values of $R$, $I_{ON}/I_{OFF}$, EQE and D* are about 80 A W$^{-1}$, 800, $2.5 \times 10^4$%, and $1.1 \times 10^{13}$ Jones, respectively (Figures S15 and S16). In addition, the van der Waals heterojunction-based FETs have a better NPC performance than that of most devices within various material systems such as nanorods, nanowires, organic semiconductors, and quantum dots (cf. Table S2).

## 2.4 | Physical Mechanisms of PPC and NPC Effects in $WSe_2$/UVO-InSe FETs

Figure 4 shows the mechanism of gate-tunable PPC and NPC effects in the $WSe_2$/UVO-InSe heterojunction-based FETs. Both ambipolar $WSe_2$ and p-type UVO-InSe are excited to generate electron-hole pairs under illumination due to the well-known photoelectric effect (cf. Figures S1d and S2). In Figure 4a, the holes in the $WSe_2$ layer migrate toward UVO-InSe under the built-in electric field ($E_{in}$) by applying $V_{GS} < V_C$. The holes in the p-type UVO-InSe contribute mainly to the channel current (cf. Figure S17a). During illumination, the photogenerated electron-hole pairs are separated by the built-in electric field and gate voltage. The number of holes in the UVO-InSe increases significantly, achieving a positive photoconductivity effect at $V_{GS} < V_C$. For the case of $V_{GS} > V_C$, the p-type characteristic of UVO-InSe is suppressed, resulting in a reduction of free holes. Meanwhile, the direction of $E_{in}$ reverses by applying a larger positive gate voltage ($V_{GS} > V_C$), as shown in Figure 4b. The major carriers in the ambipolar-type $WSe_2$ are electrons, which contribute mainly to the channel current (cf. Figure S17b). During illumination, the photogenerated holes in the p-type UVO-InSe and the electrons in the $WSe_2$ migrate to the $WSe_2$/UVO-InSe interface driven by the built-in electric field and gate voltage and then recombine. The process leads to the consumption of photogenerated and intrinsic carriers in the $WSe_2$ and UVO-InSe heterojunction. Therefore, the FET exhibits a negative photoconductivity effect at $V_{GS} > V_C$, which is confirmed by the KPFM and band alignments at $V_{GS} = 0$ V (cf. Figure S18). In addition, a pulsed laser test reveals that the $WSe_2$/UVO-InSe heterojunction-based FET exhibits a negative photoconductivity effect after illumination at $V_{GS} > V_C$ since the electrons consumed in $WSe_2$ are not replenished in time (cf. Figure S19). As the gate voltage increases from −60 to +60 V, the phototransistor exhibits a photoresponse from PPC to NPC. The corresponding dominant current distribution evolves from UVO-InSe to $WSe_2$ layer.

## 2.5 | Image Hiding and Display Based on the PPC and NPC Effects

Information security is essential for protecting personal privacy and safeguarding national security in the era of big data [7]. Figure 5 shows a real-time information protection process based on the PPC and NPC effects of a $WSe_2$/UVO-InSe heterojunction-based FET. In Figure 5a, the phototransistor acts as the platform for information protection, where the input information will be hidden by laser illumination, and then it is displayed by applying a certain $V_{GS}$ matrix. Figure 5b and Figure S20 show the photocurrent response under programmed gate voltages ($V_N/V_P$). The initially distinguishable high- and low-current states are tuned into an intermediate-current state under different laser power densities due to the NPC and PPC effects. Figure 5c illustrates an information protection process of a 7 × 7 pixelated image ("T"). Each pixel ($a_{ij}$) corresponds to an independent gate voltage $V_N$ or $V_P$ (cf. Figure S21). The image "T" will be hidden during/after illumination since the high/low current becomes an intermediate

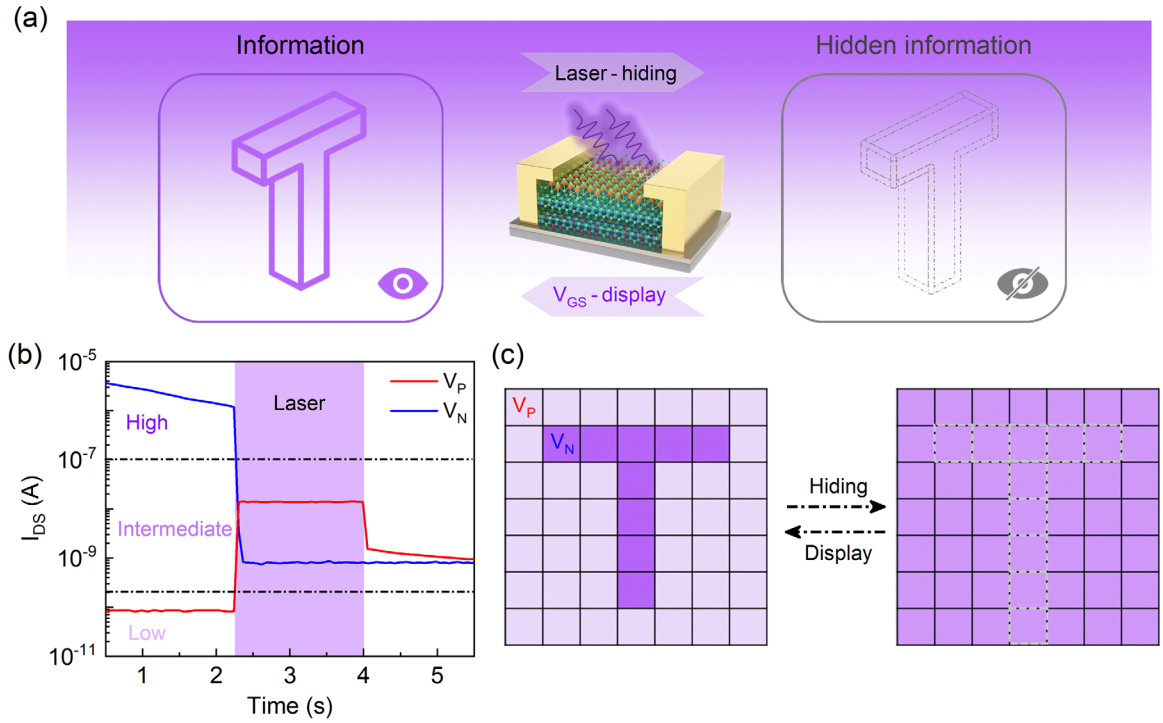


**FIGURE 5** | Information protection of the representative image "T" based on a $WSe_2$/UVO-InSe heterojunction FET. (a) Schematic illustration of information protection. (b) Photocurrent response at $V_{GS} = V_P$ and $V_{GS} = V_N$ within the three regions: Low ($I_{DS} < 2 \times 10^{-10}$ A), intermediate ($2 \times 10^{-10}$ A $< I_{DS} < 1 \times 10^{-7}$ A), and high regions ($I_{DS} > 1\ times\ 10^{-7}$ A). (c) Laser-induced image hiding and $V_{GS}$-induced display processes of the image "T".

current. Then the image "T" is displayed by applying a certain $V_{GS}$ matrix, which includes the elements $a_{ij} = V_N$ or $V_P$. Note that each pixel unit $a_{ij}$ is sequentially tested with a single FET, and the corresponding $I_{DS}(i, j)$ for each pixel unit is shown in Figure S22. Therefore, the $WSe_2$/UVO-InSe heterojunction-based FET can realize information protection by the strategy of laser-induced image hiding and $V_{GS}$-induced display.

## 2.6 | Artificial Neural Network for Pattern Recognition

Figure 6a shows a biological synapse consisting of a pre-synaptic membrane, synaptic cleft, and post-synaptic membrane. The pre-synaptic terminal releases excitatory or inhibitory neurotransmitters under light or electrical stimulation and then the neurotransmitters are transmitted to post-synaptic receptors, inducing excitatory or inhibitory postsynaptic current (EPSC/IPSC) [49, 50]. Similar to biological synapses, the $WSe_2$/UVO-InSe heterojunction-based FET shows the single- and paired-pulse PSC behaviors (cf. Figure 6b; Figure S23). It indicates that the paired-pulse facilitation (PPF) index gradually decreases from 129% to 103% with increasing laser pulse interval (cf Figure S24). Figure 6c shows the long-term potentiation (LTP) and long-term depression (LTD) by applying multi-pulsed laser and multi-pulsed gate voltage, respectively. During the potentiation process, the synaptic weight increases progressively with laser pulse number, while an opposite trend is observed during the depression process. Note that the gradual and continuous modulation of conductance suggests analog-like synaptic weight updating, which is essential for high-accuracy neuromorphic computing. In a further step, an artificial neural network (ANN) is constructed for handwritten digit recognition (cf. Figure 6d). The network architecture consists of 784 input neurons for the 28×28 pixelated grayscale image, 100 hidden neurons, and 10 output neurons. The LTP and LTD conductance states are directly mapped to the synaptic weights. The ANN is used to train and recognize handwritten digit images from the MNIST database using the CrossSim simulator. In Figure 6e, the ANN achieves a recognition accuracy of about 94.48% using experimental synaptic characteristics, which is close to that (97.64%) using ideal synaptic weights. It reveals that the as-fabricated $WSe_2$/UVO-InSe heterojunction-based FETs are capable of emulating key synaptic functions and hold potential applications for neuromorphic computing and pattern recognition.

## 3 | Conclusion

In summary, a $WSe_2$/UVO-InSe heterojunction-based FET with a reversible and stable bidirectional photoresponse has been fabricated by employing a UVO treatment on InSe nanosheets. The phototransistor exhibits a giant NPC with the $I_{OFF}/I_{ON} = 6.32 \times 10^5$ and a high negative responsivity of $R_{NPC} = -1.56{\times}10^5$ A $W^{-1}$. It is found that the accumulation and recombination of electrons and holes at the $WSe_2$/UVO-InSe interface could induce the giant NPC performance. In particular, the fundamental charge transport of the PPC performance is governed by the Ohmic conduction, while that of the NPC performance is governed by the Schottky emission conduction. Moreover, the phototransistor has an excellent PPC/NPC stability, durability, and device-to-device uniformity. Finally, information

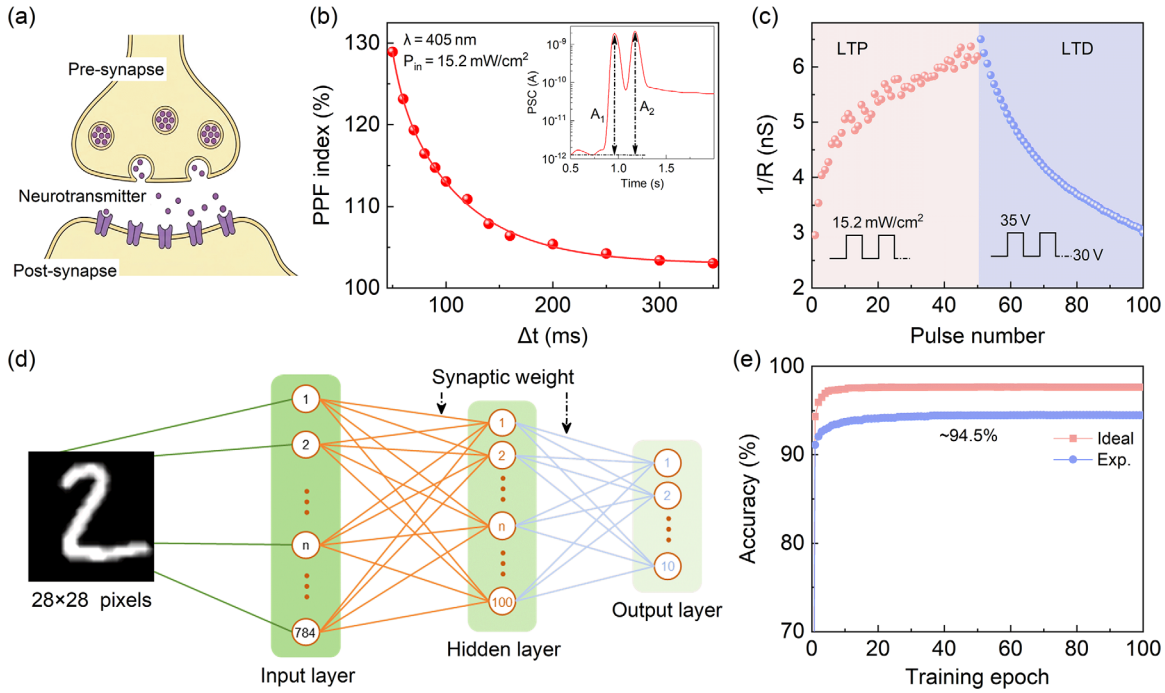


**FIGURE 6** | MNIST pattern recognition simulation of $WSe_2$/UVO-InSe heterojunction-based FETs. (a) Schematic diagrams of a biological synapse. (b) PPF index as a function of the paired pre-synaptic spike interval ($\Delta t$). Inset: PSC amplitudes ($A_1$ and $A_2$) by a pair of laser pulses. (c) Optical potentiation and electrical depression with 50 multi-pulses. (d) Schematic of an ANN structure which is simulated with the standard back-propagation algorithm. (e) Recognition accuracy as a function of training epochs for hand-written MNIST digit images.

protection and pattern recognition systems are realized based on the PPC and NPC effects. This work clarifies the physical mechanism of giant NPC performance for information protection and artificial synaptic plasticity, which represents an important step toward multifunctional neuromorphic optoelectronics.

## 4 | Experimental Section

### 4.1 | Device Fabrication

High-quality InSe and $WSe_2$ nanoflakes were mechanically exfoliated from the corresponding bulk crystals (Shanghai Onway Techology Co., Ltd) using a polydimethylsiloxane (PDMS)-assisted dry transfer method. The InSe nanosheets on PDMS were subjected to the UVO treatment, which was carried out using a commercial UVO generator. The UVO-InSe and $WSe_2$ nanosheets were sequentially transferred onto 300 nm-thick $SiO_2/p^{++}$-Si substrates. Finally, 50 nm-thick Au electrodes were deposited as source and drain contacts assisted by a shadow mask. Note that the as-fabricated devices were stored in a vacuum moisture-proof box (MVD-300N, Asone) at room temperature.

### 4.2 | Device Characterizations

The morphology and thicknesses of $WSe_2$, UVO-InSe nanosheets, and $WSe_2$/UVO-InSe heterojunctions were characterized by optical microscopy and atomic force microscopy (AFM Dimension Icon, Bruker), respectively. Raman and steady-state photoluminescence spectra were obtained by a confocal micro-Raman spectrometer (Jobin-Yvon LabRAM HR Evolution, Horiba) with the 532 nm-laser. The time-resolved photoluminescence was recorded by an avalanche photodiode with time-correlated single photon counting technique (PicoHarp 300, PicoQuant). X-ray photoelectron spectroscopy (XPS, Thermo Scientific) was carried out to analyze the chemical bonding states. Electrical measurements of the $WSe_2$, UVO-InSe, and $WSe_2$/UVO-InSe heterojunction-based FETs were performed using a Keithley 4200A semiconductor parameter analyzer in a vacuum probe station ($\sim 10^{-6}$ Torr) to minimize environmental interference. During photoelectric measurements, illumination was provided by a 405, 520, and 638 nm commercial laser (Thorlabs). Transient photocurrent was recorded with a Tektronix (DPO 5204) oscilloscope to characterize photoresponse times.

#### Author Contributions

H.G. performed the preparation of 2D layered $WSe_2$, InSe, and heterojunction-based FETs, H.G., Z.C., and Z.D. conducted the experiments for device fabrication and electrical measurements. Z.G., R.J., L.S., and J.Z. performed the detailed analysis of the physical mechanism. H.G., Z.G., J.Z., and Z.H. designed the experiments and wrote the manuscript. J.Z. supervised the research. All authors have given approval to the final version of the manuscript.

#### Acknowledgments

This work was financially supported by the National Natural Science Foundation of China (62574080, 62375086, 62574050, and 62304042), Projects of Science and Technology Commission of Shanghai Municipality (21JC1402100, 24JD1400200, and 23YF1402100), Open Fund of State Key Laboratory of Infrared Physics (SITPNLIST-YB-2024-02), Fundamental Research Funds for the Central Universities

(2025QKT001), the State Key Laboratory of Integrated Chips and Systems (SKLICS-K202510), East China Normal University Multifunctional Platform for Innovation (004), Shanghai Pilot Program for Basic Research-Fudan University (21TQ1400100 and 25TQ009), the Project of Science Technology Bureau of Shaoxing (2025B41003) and the Program for Professor of Special Appointment (Eastern Scholar) at Shanghai Institutions of Higher Learning.

## Conflicts of Interest

The authors declare no conflicts of interest.

## Data Availability Statement

The data that support the findings of this study are available from the corresponding author upon reasonable request.

## References

1. A. Dodda, D. Jayachandran, A. Pannone, et al., "Active Pixel Sensor Matrix Based on Monolayer $MoS_2$ Phototransistor Array," *Nature Materials* 21, no. 12 (2022): 1379–1387.

2. J. Schröder, A. Bonil, L. C. Winkler, et al., "Organic Permeable Base Transistors for High-Performance Photodetection with Photo-Memory Effect," *Nature Photonics* 19, no. 10 (2025): 1088–1098.

3. S. Zhang, R. Chen, D. Kong, et al., "Photovoltaic Nanocells for High-Performance Large-Scale-Integrated Organic Phototransistors," *Nature Nanotechnology* 19, no. 9 (2024): 1323–1332.

4. J. Han, W. Deng, F. Hu, et al., "2D Materials-Based Photodetectors with Bi-Directional Responses in Enabling Intelligent Optical Sensing," *Advanced Functional Materials* 35, no. 24 (2025): 2423360.

5. Y. Ke, L. Yuan, W. Xu, et al., "Ultra-Fast Weak Light Detectors Based on van der Waals Stacked 2D Semiconductor/h-BN Heterostructures," *Advanced Optical Materials* 13, no. 4 (2025): 2402226.

6. S. Wang, X. Wang, W. Wang, et al., "Unipolar Barrier Photodetectors Based on van der Waals Heterostructure with Ultra-High Light On/Off Ratio and Fast Speed," *Advanced Science* 12, no. 8 (2025): 2413844.

7. L. Liu, X. Zhang, Q. Zhang, et al., "Reconfigurable Logic of Multidimensional Encryption Based on $ReSe_2$ Homojunction Photodetector," *ACS Nano* 19, no. 27 (2025): 25490–25500.

8. H. Shao, W. Wang, Y. Zhang, et al., "Adaptive In-Sensor Computing for Enhanced Feature Perception and Broadband Image Restoration," *Advanced Materials* 37, no. 6 (2025): 2414261.

9. C.-Y. Wang, S.-J. Liang, S. Wang, et al., "Gate-Tunable van der Waals Heterostructure for Reconfigurable Neural Network Vision Sensor," *Science Advances* 6, no. 26 (2020): eaba6173.

10. C. Jin, J. Wang, S. Yang, et al., "Bidirectional Photovoltage-Driven Oxide Transistors for Neuromorphic Visual Sensors," *Advanced Materials* 37, no. 1 (2025): 2410398.

11. X. Zhang, M. Chi, S. Tian, et al., "Asymmetric Ferroelectric Gated Reconfigurable $WSe_2$ p–n Homojunction for In-Sensor Neuromorphic Vision Processing," *Advanced Functional Materials* 35 (2025): e20019.

12. Z. Zhu, L. Liu, S. Deng, and N. Xu, "Van der Waals Photonic Bipolar Junction Transistors Capable of Simultaneously Discerning Wavelength Bands and Dual-Function Chip Application," *ACS Nano* 19, no. 3 (2025): 3645–3655.

13. P. Xie, Y. Xu, J. Wang, et al., "Birdlike Broadband Neuromorphic Visual Sensor Arrays for Fusion Imaging," *Nature Communications* 15, no. 1 (2024): 8298.

14. D. Xue, W. Gong, C. Yan, et al., "Boosting Bidirectional Photoresponse with Wavelength Selectivity through Ambipolar Transport Modulation," *Advanced Functional Materials* 34, no. 38 (2024): 2402884.

15. Q. Yang, J. Hu, H. Li, et al., "All-Optical Modulation Photodetectors Based on the CdS/Graphene/Ge Sandwich Structures for Integrated Sensing-Computing," *Advanced Science* 12, no. 11 (2025): 2413662.

16. Z. Liu, Y. Wang, Y. Zhang, et al., "Harnessing Defects in SnSe Film via Photo-Induced Doping for Fully Light-Controlled Artificial Synapse," *Advanced Materials* 37, no. 4 (2025): 2410783.

17. A. Grillo, E. Faella, A. Pelella, et al., "Coexistence of Negative and Positive Photoconductivity in Few-Layer $PtSe_2$ Field-Effect Transistors," *Advanced Functional Materials* 31, no. 43 (2021): 2105722.

18. Y. Sun, Y. Wang, Z. Wang, et al., "Ambipolar $MoS_2$ Field-Effect Transistors with Negative Photoconductivity and High Responsivity Using an Ultrathin Epitaxial Ferroelectric Gate," *Advanced Functional Materials* 34, no. 37 (2024): 2402185.

19. W. He, D. Wu, L. Kong, P. Yu, and G. Yang, "Giant Negative Photoresponse in van der Waals Graphene/$AgBiP_2Se_6$/Graphene Trilayer Heterostructures," *Advanced Materials* 36, no. 16 (2024): 2312541.

20. B. Cai, Y. Huang, L. Tang, et al., "All-Optically Controlled Retinomorphic Memristor for Image Processing and Stabilization," *Advanced Functional Materials* 33, no. 46 (2023): 2306272.

21. J.-X. Qin, C.-L. Shen, L. Li, et al., "Broadband Negative Photoconductive Response in Carbon Nanodots," *Advanced Materials* 36, no. 32 (2024): 2404694.

22. Z. Gao, R. Jiang, M. Deng, et al., "Tunable Negative and Positive Photoconductance in van der Waals Heterostructure for Image Preprocessing," *Advanced Materials* 36, no. 29 (2024): 2401585.

23. Y. Tao, C. Hong, and J.-H. Kim, "Ultrafast Reversible Photoconductivity in 2D $MoTe_2$/Pt van der Waals Heterostructure," *Science Advances* 11, no. 37 (2025): eady1321.

24. T. Li, J. Miao, X. Fu, et al., "Reconfigurable, Non-Volatile Neuromorphic Photovoltaics," *Nature Nanotechnology* 18, no. 11 (2023): 1303–1310.

25. X. Huang, Y. Su, J. Dong, et al., "Unveiling Distinct Ultrafast Photocarrier Dynamics and Tailored Nonlinear Optical Absorption in Phase-Engineered Two-Dimensional $MoTe_2$," *ACS Nano* 19, no. 37 (2025): 33644–33654.

26. P. Guo, M. Jia, D. Guo, T. Ren, Z. L. Wang, and J. Zhai, "Progress in Flexoelectric Effect Research and Related Applications," *SmartSys* 1, no. 1 (2025): e1.

27. S. Ghosh, A. Varghese, H. Jawa, Y. Yin, N. V. Medhekar, and S. Lodha, "Polarity-Tunable Photocurrent through Band Alignment Engineering in a High-Speed $WSe_2$/$SnSe_2$ Diode with Large Negative Responsivity," *ACS Nano* 16, no. 3 (2022): 4578–4587.

28. J. Deng, D. Guo, Y. Wen, et al., "Evidence of Ferroelectricity in an Antiferromagnetic Vanadium Trichloride Monolayer," *Science Advances* 11, no. 10 (2025): eado6538.

29. X. Feng, R. Cheng, L. Yin, Y. Wen, J. Jiang, and J. He, "Two-Dimensional Oxide Crystals for Device Applications: Challenges and Opportunities," *Advanced Materials* 36, no. 2 (2024): 2304708.

30. T. Kang, Z. Lu, L. Liu, et al., "In-Situ Defect Engineering of Controllable Carrier Types in $WSe_2$ for Homomaterial Inverters and Self-Powered Photodetectors," *Nano Letters* 23, no. 23 (2023): 11034–11042.

31. L. Philpott, B. C. Johnson, M. Fronzi, et al., "Strain-Dependent Photodetection with Layered InSe Photoconductors," *Nano Letters* 25, no. 24 (2025): 9526–9534.

32. P. Guo, M. Jia, D. Guo, Z. L. Wang, and J. Zhai, "Retina-Inspired In-Sensor Broadband Image Preprocessing for Accurate Recognition via the Flexophototronic Effect," *Matter* 6, no. 2 (2023): 537–553.

33. W. Li, Q. Qin, X. Li, et al., "Robust Growth of 2D Transition Metal Dichalcogenide Vertical Heterostructures via Ammonium-Assisted CVD Strategy," *Advanced Materials* 36, no. 46 (2024): 2408367.

34. R. Xu, L. Song, X. Li, et al., "A Two-Dimensional NiS/$MoS_2$ Metal-Semiconductor Vertical Heterojunction for a Sub-100 nm Transistor," *ACS Nano* 19, no. 28 (2025): 25870–25878.

35. X. Chen, H. Zhao, R. Fei, et al., "Efficient Energy Transfer in a Hybrid Organic-Inorganic van der Waals Heterostructure," *Science Advances* 11, no. 36 (2025): eadw3969.

36. R. Choudhary and B. Jalan, "Atomically Precise Synthesis of Oxides with Hybrid Molecular Beam Epitaxy," *Device* 3, no. 3 (2025): 100711.

37. Z. Cheng, Z. Hong, Z. Li, et al., "Channel-Type Engineering in an InSe-Based Transistor: Paving a Way for Next-Generation Reconfigurable Electronics," *Nano Letters* 25, no. 36 (2025): 13647–13654.

38. D. Lee, Y. Choi, J. Kim, and J. Kim, "Recessed-Channel $WSe_2$ Field-Effect Transistor via Self-Terminated Doping and Layer-by-Layer Etching," *ACS Nano* 16, no. 5 (2022): 8484–8492.

39. M. Uzhansky, S. Mukherjee, G. Vijayan, and E. Koren, "Non-Volatile Reconfigurable p–n Junction Utilizing In-Plane Ferroelectricity in 2D $WSe_2/\alpha$-$In_2Se_3$ Asymmetric Heterostructures," *Advanced Functional Materials* 34, no. 8 (2024): 2306682.

40. Y. Zhao, J. Cho, M. Choi, et al., "Light-Tunable Polarity and Erasable Physisorption-Induced Memory Effect in Vertically Stacked InSe/$SnS_2$ Self-Powered Photodetector," *ACS Nano* 16, no. 10 (2022): 17347–17355.

41. C. Zhao, Z. Gao, Z. Hong, et al., "Ferroelectric and Optoelectronic Coupling Effects in Layered Ferroelectric Semiconductor-Based FETs for Visual Simulation," *Advanced Science* 12, no. 11 (2025): 2413808.

42. Y. Zou, Z. Zhang, J. Yan, et al., "High-Temperature Flexible $WSe_2$ Photodetectors with Ultrahigh Photoresponsivity," *Nature Communications* 13, no. 1 (2022): 4372.

43. C.-M. Yang, T.-C. Chen, D. Verma, et al., "Bidirectional All-Optical Synapses Based on a 2D $Bi_2O_2Se$/Graphene Hybrid Structure for Multifunctional Optoelectronics," *Advanced Functional Materials* 30, no. 30 (2020): 2001598.

44. K.-H. Li, X.-Y. Zhang, L.-Y. Hu, et al., "Wavelength-Controlled Triple-Mode Photoconductance-Polarity-Switching Field-Effect Transistor for Secure Time-Variable Encrypted Optical Communication," *ACS Nano* 19, no. 19 (2025): 18607–18619.

45. W. Li, T. Mu, P. Li, et al., "Reconfigurable Floating-Gate Devices with Ambipolar $ReSe_2$ Channel: Dual-Mode Storage, NMOS-PMOS Transformation, Logic Functions, Synapse Simulations, Positive and Negative Photoconductive Effects," *Advanced Functional Materials* 35, no. 42 (2025): 2425359.

46. J. Jiang, W. Xu, Z. Sun, et al., "Wavelength-Controlled Photoconductance Polarity Switching via Harnessing Defects in Doped $PdSe_2$ for Artificial Synaptic Features," *Small* 20, no. 13 (2024): 2306068.

47. Y. Wang, E. Liu, A. Gao, et al., "Negative Photoconductance in van der Waals Heterostructure-Based Floating Gate Phototransistor," *ACS Nano* 12, no. 9 (2018): 9513–9520.

48. C. Zhu, H. Liu, W. Wang, et al., "Optical Synaptic Devices with Ultra-Low Power Consumption for Neuromorphic Computing," *Light: Science & Applications* 11, no. 1 (2022): 337.

49. Q. F. Wang, R. Q. Jiang, Z. T. Gao, et al., "A $HfS_2$-Based Photoelectronic Synaptic Transistor with Tunable Synaptic Plasticity for Emotional Memory," *Applied Surface Science* 613 (2023): 156148.

50. H. Jiang, H. Ji, Z. Ma, et al., "Simultaneously Achieving Negative Photoconductivity Response and Volatile Resistive Switching in $Cs_2CoCl_4$ Single Crystals towards Artificial Optoelectronic Synapse," *Light: Science & Applications* 13, no. 1 (2024): 316.

## Supporting Information

Additional supporting information can be found online in the Supporting Information section.

**Supporting File**: adfm75409-sup-0001-SuppMat.pdf.